IOP Publishing Journal of Physics D: Applied Physics

J. Phys. D: Appl. Phys. **55** (2022) 415204 (14pp) https://doi.org/10.1088/1361-6463/ac855d

Analysis of a nano-pulsed DBD Plasma jet for endoscopy and impact of excitation parameters

Orianne Bastin[1,2,*], Max Thulliez[1,2], Alain Delchambre[1], Jacques Devière[3], François Reniers[2] and Antoine Nonclercq[1]

[1] Bio-, Electro- and Mechanical- system (BEAMS), Biomed Group, Ecole polytechnique de Bruxelles, Brussels, Belgium
[2] Faculty of Sciences, Chemistry of Surfaces, Interfaces, and Nanomaterials, ChemSIN, Université libre de Bruxelles, Brussels, Belgium
[3] Department of Gastroenterology, Hepatopancreatology, and Digestive Oncology, C.U.B. Erasme Hospital, Université Libre de Bruxelles, Brussels, Belgium

E-mail: Orianne.Bastin@ulb.be

Received 24 May 2022, revised 18 July 2022
Accepted for publication 29 July 2022
Published 18 August 2022

Abstract

Cold atmospheric plasma induces various dose-dependent effects on living cells, from proliferation to necrosis. These effects are of interest in the field of therapeutic flexible endoscopy, although implementing an effective plasma delivery system represents a technical challenge. This work studies the impact of critical parameters on plume intensity, delivered reactive species (RS), and current administered to the target for the use of plasma in endoscopy. A 2 m long dielectric barrier discharge plasma jet was studied upon nano-pulsed high voltage excitation to increase plasma reactivity. The peak voltage, gas gap, pulse repetition frequency, and pulse width were varied while the power dissipated by the system and the optical emissions (with imaging and spectrometry) were measured. Two configurations were compared: the first one with the plume exiting freely in air, and the second one with the plume impinging an electrical equivalent of the human body. Finally, the current flowing through the capillary was measured at regular intervals along the tube with a Rogowski coil. Results show that (a) a conductive target increases the ratio of RS produced over the dissipated power, (b) increasing the pulse repetition frequency does not improve the RS production per pulse (e.g. through a synergetic, memory effect), (c) increasing the pulse width does not influence RS production but increases the dissipated power, and (d) current linearly leaks through the tube walls, and leaks are lower with nano-pulsed compared to sinusoidal excitation. Reactance and capacitance values of the system are analyzed based on the electrical equivalent circuit approach. Finally, displacement and discharge currents are discussed to bring power dissipation mechanisms to light and compare them between configurations. The conclusions drawn are important for the future design of safe and effective endoscopic plasma devices.

Keywords: cold atmospheric plasma, endoscopy, electrical characterization, pulsed voltage, dissipated power, discharge, displacement

(Some figures may appear in colour only in the online journal)

* Author to whom any correspondence should be addressed.

1. Introduction

Cold atmospheric plasma (CAP) for medical applications has been a field of interest over the last two decades [1, 2]. The reactive species (RS) produced by CAP have various biological effects on cells, such as the triggering of programmed cell death (apoptosis), the promotion of cell proliferation, or the induction of selective death of cancer cells [3–5]. It could, therefore, represent an interesting tool for the treatment of malignant or dysplastic lesions [6, 7], the promotion of wound healing [8], cell regeneration [8], or for achieving hemostasis [9]. Some of these projects have already led to the development of medical devices, such as the kINPenMED® (neoplas tools GmbH) and the PlasmaDerm® (CINOGY System GmbH), which are currently available on the market [10] or are protected by patents [11, 12].

Progress in flexible therapeutic endoscopy has allowed for the treatment of an increasing number of pathologies through endoluminal, minimally invasive surgery [13–16]. Consequently, systems aiming to deliver cold plasma through a flexible endoscope have been proposed over the last decade [17–20]. However, the practical implementation of these systems must comply with major technological and medical constraints. In addition to the geometric requirements of the gastrointestinal tract, the plasma reactivity (linked to the amount of ROS produced) must be maintained at the treatment site while limiting current administration to the patient [21]. Due to their intrinsic configuration, dielectric barrier discharges (DBD) are often used to build plasma jet reactors for endoscopy. The dielectric barrier limits the current flowing through the plasma and allows for a homogeneous discharge at room temperature, suitable for heat-sensitive tissues [22, 23]. In this context, a better understanding of DBD plasma reactor behavior and how to predict that behavior is necessary to optimize, monitor, and control DBD plasma medical devices [24].

When used in medicine, the plasma jet should be effective (i.e. induce a biological response) but at the same time safe (i.e. not harm the patient through administration of excessively high current) [25]. Therefore, the high excitation voltage used to generate the plasma is a critical parameter as it is directly linked to both effectiveness and safety [10]. To compare different excitation voltage waveforms (e.g. pulsed versus sine waves) and their effect, the active power dissipated by the system is usually computed simultaneously to plasma reactivity [26–28]. Walsh *et al* have reported that a pulsed atmospheric-pressure glow discharge produces more ROS with five times lower power consumption than with sinusoidal excitation [26]. For excimer DBD lamps, Mildren *et al* obtained 3.2 times better efficiency in terms of emission intensity [27]. Finally, Ayan *et al* observed a more homogeneous discharge with a nanopulsed signal compared to a micropulsed signal [28].

In DBD, this active power is dissipated either by the discharge itself (e.g. gas heating, ionization, light emission, RS production) or by dielectric heating [29]. This latter is characterized by the dielectric loss tangent $(\tan\delta)$ coefficient. For sinusoidal voltage applied to a plasma actuator, it is proportional to the square of the peak voltage and to the frequency [29]. Several groups have compared the dielectric thermal power with the total active power (dissipated in the system) and found that it is significant, especially when the applied voltage is kept close to the breakdown value [30, 31]. By lowering the power dissipated by the dielectric, it is, therefore, possible to maximize the ratio of plasma reactivity over power consumption.

When a DBD plasma system is operated with a pulsed excitation voltage, two current pulses appear for each voltage pulse, at the voltage rise and fall times, respectively [26, 32, 33], as a voltage variation is needed to allow current flow through a DBD system. For a positive voltage pulse, the first current pulse has a positive polarity and the second one has a negative polarity. There are, therefore, two essential timescales for studying pulsed plasma: the *pulse repetition frequency (f)* (i.e. the time between successive voltage pulses), and the voltage *pulse width (pw)*, linked to the time between two current pulses.

With these recent findings on atmospheric plasma jets [18, 34, 35], there is now a need to characterize a long plasma jet operated with pulsed voltage to optimize potential endoscopic applications. This article assesses the impact of peak applied voltage, pulse repetition frequency and pulse width on plasma reactivity and dissipated power. In addition, the target (i.e. free jet or human electrical equivalent) and the jet-to-target distance are varied to evaluate various treatment conditions. Finally, the current leaks along the system are measured and compared with a similar system excited with sinusoidal voltage.

2. Experimental

2.1. Plasma reactor

The single electrode DBD plasma jet is depicted in figure 1. It consists of a tubular DBD-chamber made of quartz (outer diameter of 7 mm, inner diameter of 5 mm), connected upstream to a helium gas cylinder, an admission valve, and a flowmeter. The high voltage electrode consists of a copper tape wrapped around the chamber over 4 cm. The chamber is plugged into a polytetrafluoroethylene (PTFE) tube, transporting the plasma post-discharge over 2 m. The PTFE tube has an outer diameter of 3 mm, fitting in an endoscope, and a wall thickness of 0.75 mm to ensure electrical insulation. A heat-shrinkable insulating sleeve makes the fluidic connection between the quartz chamber and the PTFE capillary. A copper rod (0.8 mm diameter), maintained at the center by two machined PTFE parts, extends inside the quartz chamber and is soldered to a copper wire (0.2 mm diameter), both at floating electrical potential. This latter extends inside the PTFE capillary up to 5 mm before the end of the capillary. In this system, plasma is ignited at two different places. Indeed, when helium is flushed into the quartz chamber, plasma appears between the electrode and the floating copper rod. Then, helium re-ignites at the end of the capillary, where the copper wire stops in a configuration similar to corona discharges.

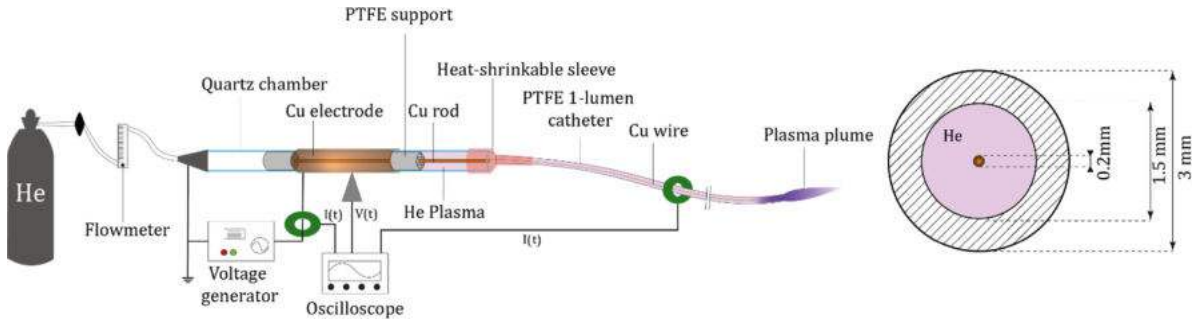

Figure 1. Schematic of the plasma system, with probes positions (left) and catheter section (right).

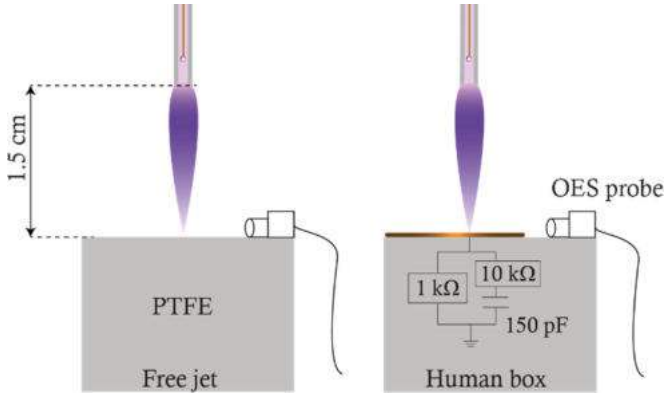

Figure 2. Plasma plume configuration and OES probe position. Free jet (left) and human box (right).

The pulsed high-voltage source is an NSP 120–20 k generator from Eagle Harbor Technologies (EHT). It generates positive polarity pulses, with a maximum voltage of 20 kV, a pulse repetition frequency up to 10 kHz, and pulse width ranging from 40 ns to 500 ns, all individually adjustable.

To mimic the electrical impedance of the human body, an *electrical equivalent human body* target based on the work of Stancampiano *et al* [36, 37] was built and placed at the output of the PTFE tube. This target, referred to as the 'human box' in this paper, consists of a box with a copper disk connected to an electrical circuit, as shown in figure 2. The 'human box' is connected to ground. The gas gap is defined as the gap between the capillary end and the target.

2.2. Measurement setup

Plasma plumes were visually compared. Pictures were taken with a Nikon D90+ camera operating in manual mode, manual focus, ISO 1000, shutter speed 1 s, and focal length 8 in a dark room. Mean pixel intensity was computed with ImageJ software over the entire picture area.

Optical emission spectroscopy (OES) was carried out with an Andor Technology SR-500i-D2-R spectrometer to understand better the plasma composition, with an acquisition time of 2 s repeated three times. The probe position is shown in figure 2. Based on the work of Chen *et al* [38], five major lines of the most relevant species were selected and used for analysis: helium peak at 706.52 nm ($He\left(3^3S \rightarrow 2^3P\right)$) to assess the presence of helium excited species, as it has been reported to be linked to energetic electrons in atmospheric plasma [39–41], $OH \bullet (A - X)$ band at 309 nm, and O peak at 777.19 nm ($O(^5P) \rightarrow O(^5S)$) for reactive oxygen species, N_2 $(C - B)$ second positive band at 337.05 nm and $N_2{}^+$ $(B - X)$ first negative system band at 391.35 nm for reactive nitrogen species. At those wavelengths, the light intensity was recorded and used to draw one graph for each wavelength of interest, with light intensity on the *y*-axis and the parameter studied on the *x*-axis.

The whole parameter space of the high-voltage source generator (0–20 kV peak voltage, 1–10 kHz pulse repetition frequency, and 40–500 ns pulse width) is not accessible and depends on the load. In that regard, its measured output voltage may differ from the nominal voltage. Current and voltage were monitored at the output of the voltage generator with a WaveSurfer 3024z (bandwidth of 200 MHz, sample rate of 4 GS s^{-1}, memory of 10 Mpts ch^{-1}) oscilloscope connected to a high-voltage probe (Tektronix P6015A x1000 3pF 100 MOhms) placed at the high-voltage electrode (represented as a triangle in figure 1). Two current monitors (Rogowski coil Pearson model 2877 output 1 V A^{-1} and 6595 output 2 V A^{-1}) were placed between the generator and the high voltage electrode and along the PTFE tube (see the green circles, figure 1).

When relevant, RMS currents were computed using the root-mean-square function on MATLAB™ over an entire number of periods [42].

In addition, the instantaneous power delivered to the whole system was computed as:

$$P_i\left(t\right) = V_a\left(t\right).I_{tot}\left(t\right). \tag{1}$$

The power dissipated in the device was deduced by averaging this power over an entire number of periods. The number of periods for averaging was chosen depending on the time-window size recorded, the time resolution of the oscilloscope, and the file size. Nineteen and nine periods were selected for a voltage pulse repetition frequency of 10 and 2 kHz, respectively.

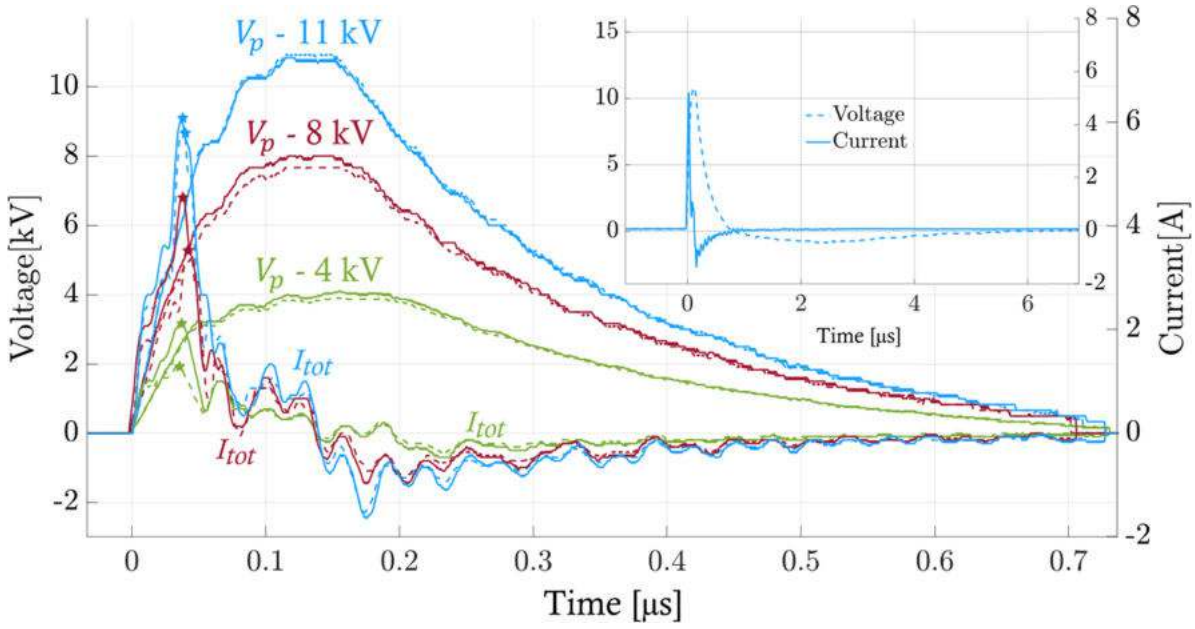

Figure 3. Comparison of input voltage and input current between free jet and human box configurations, for different values of peak voltage (4, 8, and 11 k V). Dashed lines are for the free jet configuration and solid lines for the human box configuration. Stars show the maximum of the current main peak for each curve. Longer timescale is shown in the upper right corner.

2.3. Experimental protocol

Four key parameters were studied based on their influence on plasma reactivity, as described for different systems by [43–45]:

(a) the peak voltage V_p (from 4 to 11 kV),
(b) the gas gap d (from 0.5 to 2.5 cm) when the plasma plume is impinging the human box (i.e. the gap between the capillary outlet and the target),
(c) the voltage pulse repetition frequency f (from 2 to 10 kHz),
(d) the pulse width pw (from 100 to 400 ns).

When relevant, two configurations were studied: the free jet configuration, with the plume in the open air only, and the human box configuration, with the plume being applied to the human box.

The outputs of the measurements were (a) the power dissipated in the whole system, (b) the plume pictures and their mean pixel intensity (over the entire picture), and (c) the OES peaks/bands values. In addition, the current evolution along the tube was measured to assess the current leak through the PTFE wall.

The system characterization was conducted around one nominal set of intermediary stimulation parameters ($V_p = 11$ kV, $pw = 100$ ns, $f = 10$ kHz, $d_g = 1.5$ cm).

3. Results

3.1. Impact of the high-voltage generator peak voltage

The influence of the peak voltage on the power dissipated in the system and the amount of RS produced was investigated for both configurations (the free jet mode and the human box mode). The pulse repetition frequency was set at 10 kHz, the pulse width at 100 ns, with a gas gap of 1.5 cm. Input voltage and current are presented in figure 3.

The input voltage and current remained relatively similar for the free jet or human box configurations, except for the height of the main positive current pulse, which was higher (difference from 0.2 to 1 A) for the human box. Figure 4 shows the optical emission spectra obtained in free jet, for several applied peak voltages. As explained in previous section, five lines of interest (highlighted on figure 4) were used to draw figure 5 in order to compare experiments. Figures 6 and 7 show the plasma plume pictures, and the dissipated power, respectively, as a function of the peak voltage for both configurations. When the peak voltage increased in the free jet configuration, the plume intensity and the dissipated power increased linearly (dashed lines in figure 8). In contrast, with the human box, the impact of the peak voltage on emission (OES or plume pictures) was not linear. Indeed, above a given voltage, the plasma discharge regime changed, and a much more luminescent discharge was observed while the input power increased relatively linearly. At high input voltage, much more RS were produced with the human box compared to the free jet, for a relatively similar input power. For instance, at 11 kV, for a 10% dissipated power increase due to the human box (5.4 vs. 4.9 W in free jet), the peak heights of OH, N_2, N_2^+, He, and O were multiplied by 26, 7, 3, 2.5, and 9, respectively.

3.2. Impact of the gas gap

The influence of the gas gap (in cm) between the capillary end and the target was studied. There is a direct link with the previous section since, when using the human box configuration, increasing the distance between the capillary end and the

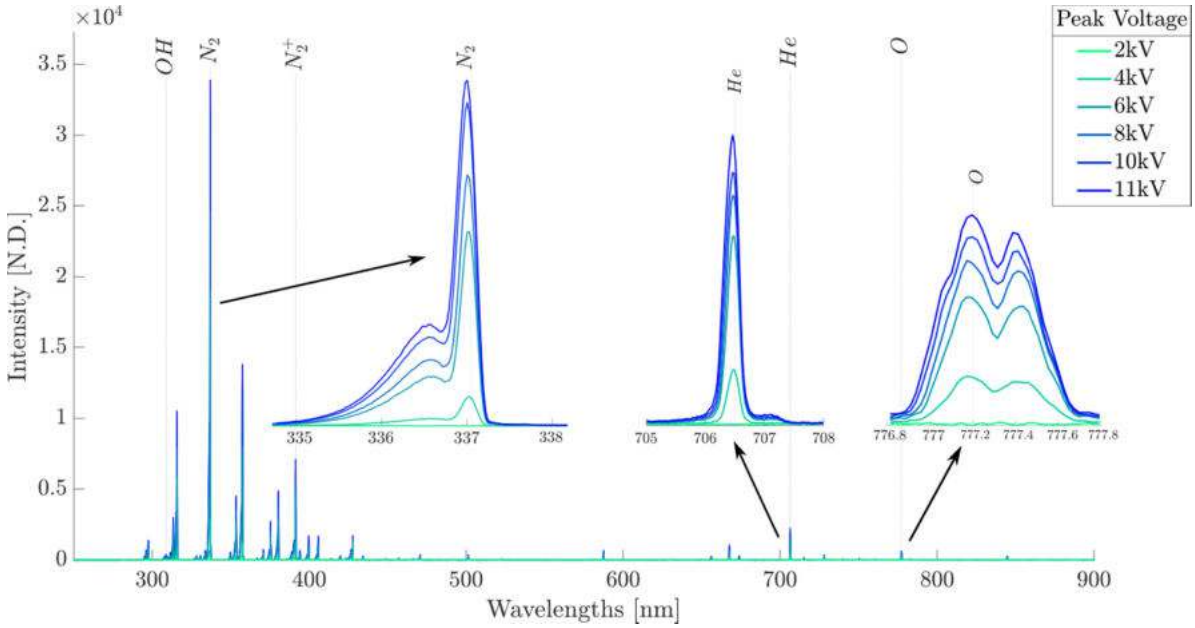

Figure 4. Optical emission spectra for several peak voltages (in free jet) with zooms on wavelengths of interest (337.05, 706.52 and 777.19 nm). Values reported in figure 5 correspond to the maxima of those spectra at those wavelengths.

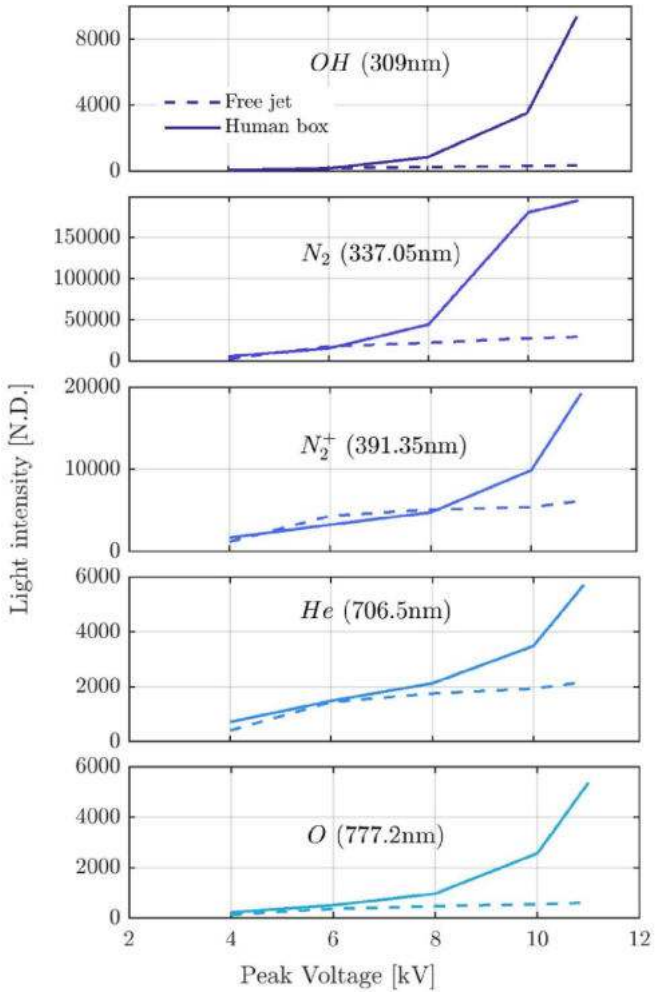

Figure 5. OES peak intensity for several emission bands as a function of the peak voltage of the pulses.

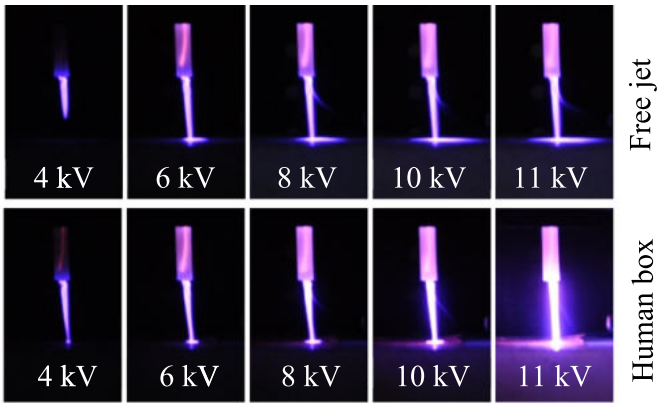

Figure 6. Plume pictures with increasing peak voltage of the pulse.

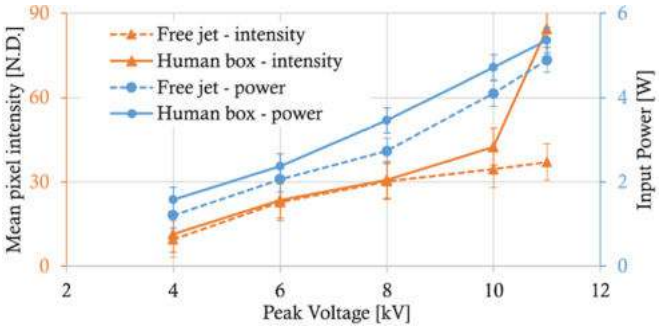

Figure 7. Mean pixel intensity and power dissipated by the device as a function of the peak voltage applied for free jet (solid line) and human box (dashed line) configurations. Power was averaged on 19 periods.

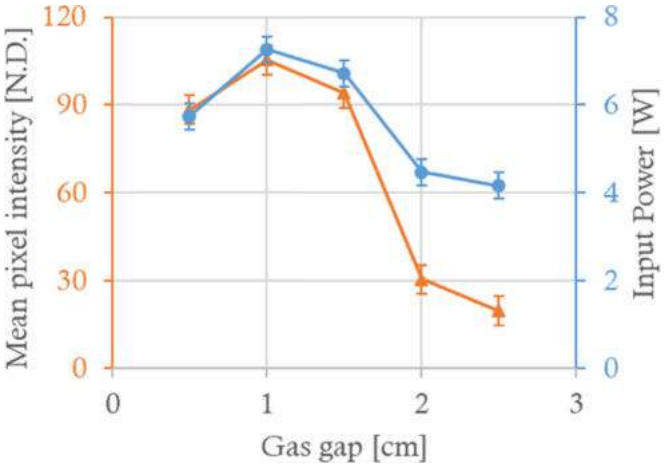

Figure 8. Mean pixel intensity (triangle) and power (circle) dissipated by the device as a function of the gas gap, for the human box configuration. Power was averaged on 4 periods.

human box eventually ends up in a large gas gap, similar to a free jet. This distance influences the dissipated power and the species produced. The peak voltage, pulse width, and frequency were equal to 11 kV, 100 ns, and 10 kHz, respectively.

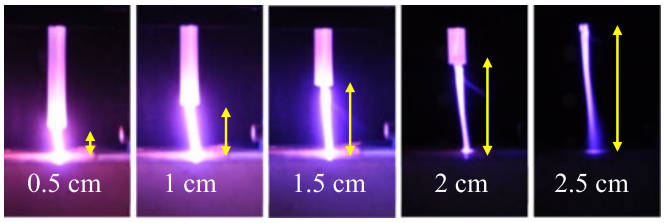

Figure 9. Plume pictures as a function of the gas gap, with the human box.

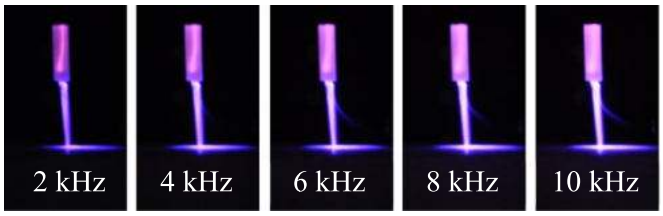

Figure 10. Plume pictures when the repetition frequency of the pulses increases, free jet configuration.

Figures 8 and 9 show the mean pixel intensity with dissipated power and the plume pictures, respectively, obtained for distances from 0.5 to 2.5 cm.

As already described for sinusoidal excited plasma [46], we observed a clear transition between two plasma regimes for a distance greater than 1.5 cm between the capillary and the human box. This is highlighted in pictures and by the power dissipated in the system (figures 8 and 9).

3.3. Impact of the pulse repetition frequency

To evaluate whether the time between successive pulses influences the dissipated power or the formation of RS in the free jet configuration, the pulse repetition frequency was increased from 2 to 10 kHz. Peak voltage and pulse width were set at 11 kV and 100 ns, respectively. Plume pictures (figure 10) qualitatively showed an increasing intensity with frequency, quantitatively confirmed by the mean pixel intensity and input power (figure 11).

Similarly, as highlighted by OES (figure 12), the emission intensity of RS increased linearly with the pulse repetition frequency within the range of screened frequency. This means that a shorter time between successive pulses does not favor the production of species. For instance, increasing the repetition rate by five also increased the production of species roughly by five. More precisely, a repetition of 10 000 pulses per second emits 4.9 times more OH (309 nm), 5.2 times more N_2 (337.05 nm) and N_2^+ (391.35 nm), 5.5 times more He (706.5 nm) and 4.5 times more O (777.19 nm) than 2000 pulses per second.

3.4. Impact of the pulse width

In this section, the influence of the pulse width is presented. The peak voltage (height of the pulse) was set at 7.5 kV,

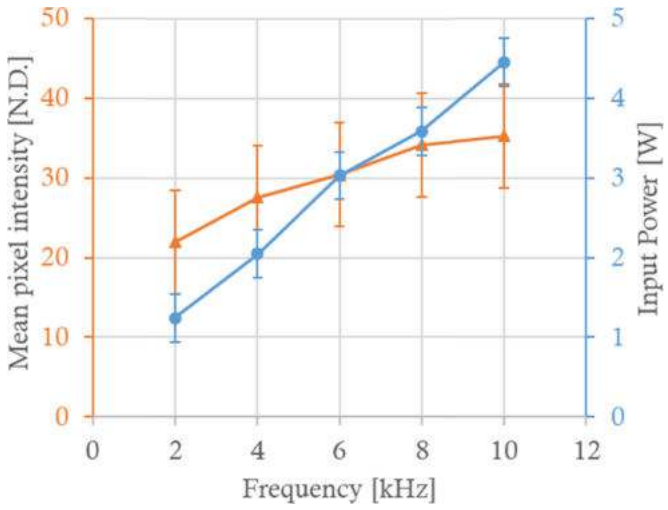

Figure 11. Mean pixel intensity (triangle) and power (circle) dissipated by the device as a function of the pulse repetition frequency, free jet configuration. Power was averaged on nine periods.

and the frequency was set at 10 kHz. The peak voltage value differed from the nominal value used for other sections due to technical limitations of the generator (i.e. the generator could not maintain a pulse for 400 ns at 11 kV).

Figure 13 shows the applied input voltage and the resulting input current. Two large current peaks are visible. The first one, positive, appears during the voltage rise slope and the second one, negative, when the voltage falls from its peak value, as previously reported by several groups [32, 33, 47]. The first current peak is similar for all pulse widths, which was expected since voltage rise slopes are similar for all pulse widths (i.e. a rising time of 100 ns to reach a nominal input voltage of 7.5 kV). However, the negative current pulse differed depending on the width, since it appeared when the applied voltage fell (at time t_1, t_2, t_3, t_4, for input voltage pulse widths of 100, 200, 300 and 400 ns, respectively).

Figure 14 compares the mean pixel intensity of plume pictures with the input power. Interestingly, the power dissipated by the device increased with the pulse width while the amount of RS produced did not, as indicated by the mean pixel intensity. Similarly, the OES peaks (in figure 15) of the different RS were relatively constant as a function of the pulse width.

It can be seen in figure 13 that, during the voltage pulse rise (before t_1), the instantaneous power dissipated was equal for each pulse width, since both the input voltage and input current were identical. Therefore, the additional dissipated power was either occurring (a) after the voltage pulse rise (i.e. after t_1) and while it was maintained at its maximum value (i.e. before t_i, i being the studied pulse width), while the input current shows positive oscillations, or (b) related to the second current pulse (i.e. right after t_i), which would require more power for a longer time between voltage rise and fall, due to a memory effect.

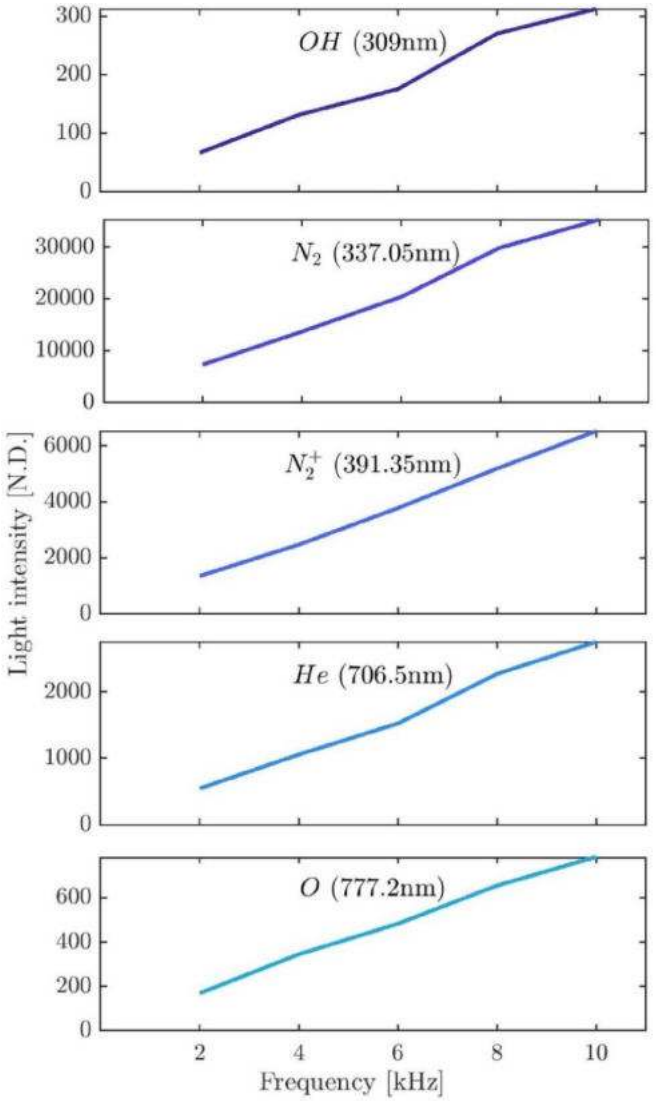

Figure 12. OES peak intensity for several emission bands as a function of the pulse repetition frequency, free jet configuration.

3.5. Current evolution along the tube

The instantaneous current flowing through the device was measured along the tube at 20 cm intervals from the high voltage electrode (with a Rogowski placed around the capillary, see figure 1), and the RMS value was computed over 19 periods. The pulse width, repetition frequency, peak voltage, and gas gap were set at 100 ns, 10 kHz, 11 kV, and 1 cm, respectively. Figure 16 shows the current evolution along the tube for both configurations. The RMS current values decreased by an average of 0.21 mA cm^{-1}. Based on this constant decrease, the RMS current at the plume (i.e. at 200 cm from the electrode) would reach roughly 10 mA. Interestingly, the RMS current flowing in the device was relatively similar when the plume was in free jet or with the human box; the dissipated power being only about 10% higher with the human box (5.5 W compared to 4.9 W with the free jet). This contrasts

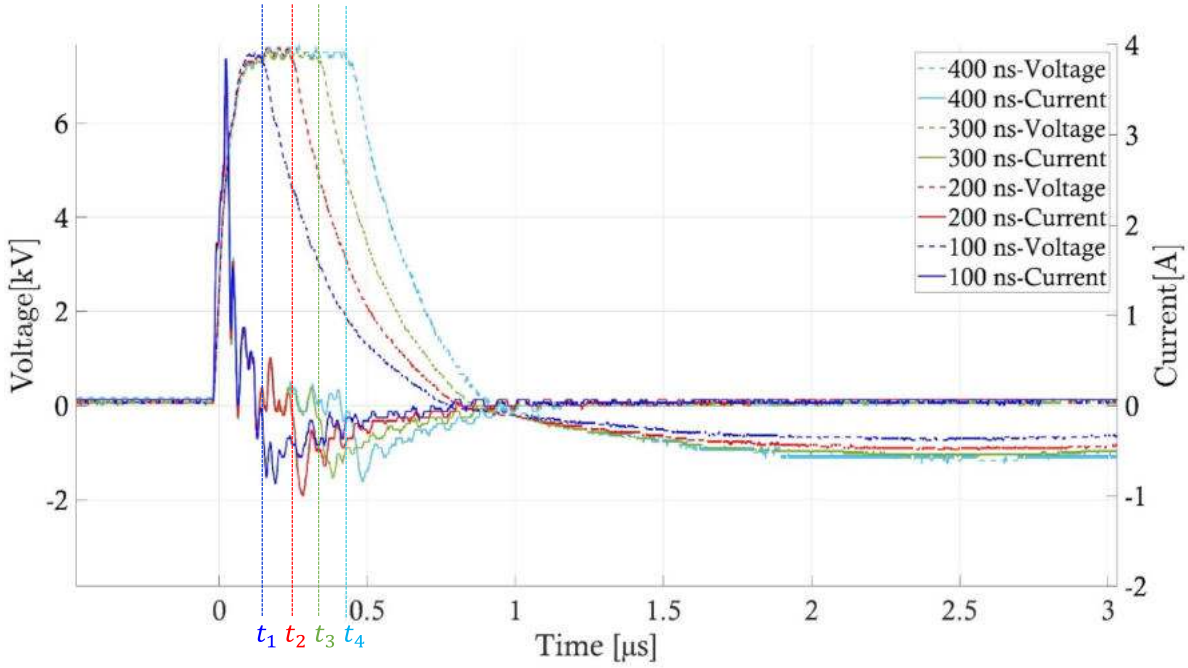

Figure 13. Input voltage (dashed lines) and current (solid lines) for different pulse widths, in free jet. t_1 to t_4 correspond to applied voltage fall (depending on the pulse width).

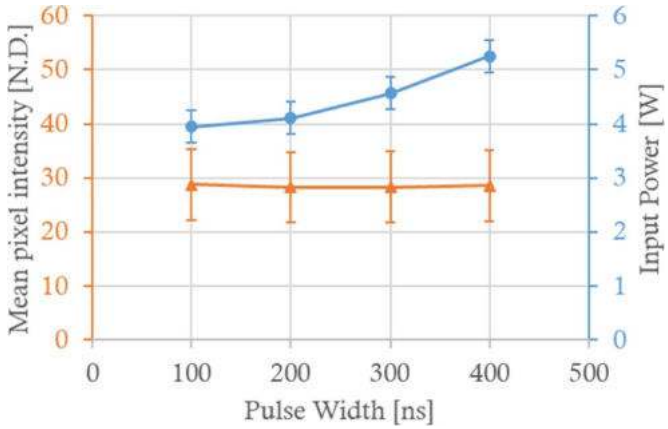

Figure 14. Mean pixel intensity (triangle) and power (circle) dissipated by the device as a function of the pulse width, free jet configuration. Power was averaged on 19 periods.

with the mean pixel intensity which was drastically higher (21 with the human box versus 12 in free jet), as already observed in figure 7.

4. Discussion

This work studied the behavior of a 2 m long DBD plasma jet device intended for endoscopic use and excited with a pulsed input voltage. When relevant, two target configurations were compared: the free jet, where the plasma plume diffuses freely outside the capillary, and the human box, in which the plasma plume hits an electrode connected to a human body electrical equivalent connected itself to ground.

The electrical behavior of this system can be discussed based on its electrical equivalent circuit, schematically shown in figure 17(a). V_a and I_{tot} are the applied voltage and the total current, respectively. C_d, C_g, and R_p are the dielectric capacitance (of quartz and the PTFE tube wall), the gas capacitance (between the quartz wall and the copper rod first, and then between the tip of the copper wire and the target), and the plasma time-variable resistance [48, 49] (again, at both ends of the copper central rod or wire), respectively [50]. ESR stands for equivalent series resistance and represents the dielectric losses in the quartz barrier. Based on materials ($\varepsilon_{r-quartz} = 3.7$ and $\varepsilon_{r-PTFE} = 2.1$) and system geometry, the dielectric capacitances were estimated: $C_{dquartz} = 24\ pF$ and $C_{dPTFE} = 337\ pF$.

Finally, I_{disp} and I_{disch} stand for displacement and discharge currents [33, 50]. The former is the capacitive current flowing through the system without plasma ignition (when plasma is off and R_p is very high). The latter results directly from the discharge ignition (sometimes referred to as conductive current). In a traditional plasma reactor, with two electrodes and one dielectric layer, separated by only one gas gap [51–53], the total input current is simply the sum of the displacement and discharge currents. The former can be deduced by knowing the capacitance of the gas gap (from its geometric and electrical characteristics). The discharge current can then be determined by subtracting the displacement current from the total current. In our system, as seen on the electrical equivalent circuit (figure 17(a)), intermittent plasma ignition appears in two places (in the quartz chamber and at the plume). Hence discharge and displacement currents both appear twice and cannot be disentangled from the total current by simple subtraction. In addition, as there is a current leak through the

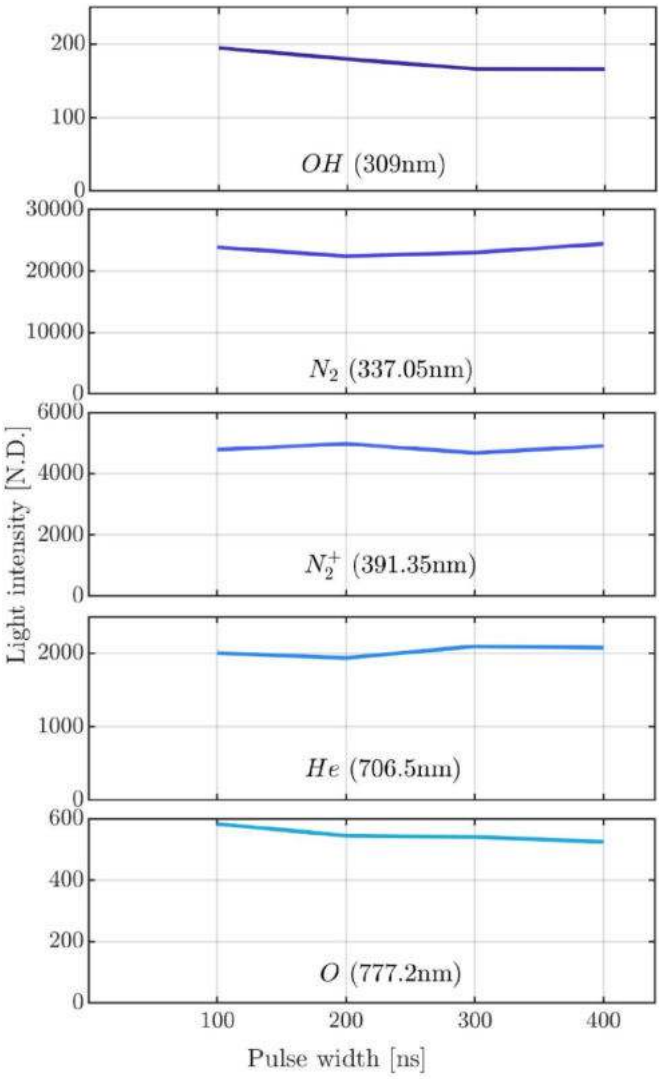

Figure 15. OES peak intensity for several emission bands as a function of the pulse width, free jet configuration.

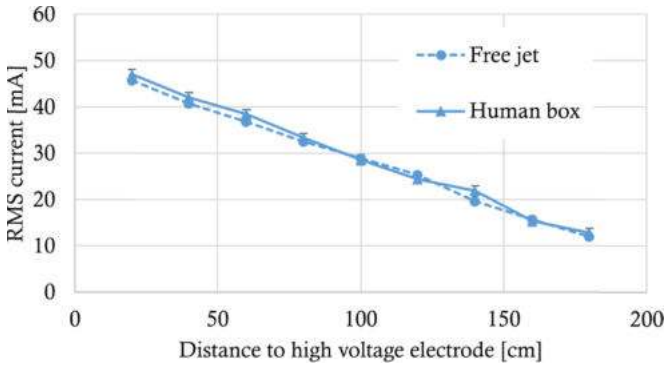

Figure 16. RMS current measured along the capillary as a function of the distance between high voltage electrode and the measure point, for free jet configuration.

PTFE wall along the whole capillary, it is not possible to measure either the sum of discharge and displacement currents in the quartz chamber (i.e. $I_{\text{disch1}} + I_{\text{disp1}}$), or at the plume (i.e. $I_{\text{disch2}} + I_{\text{disp2}}$). However, figure 17(a) is interesting to discuss qualitatively the results presented in this article, even if all currents are not fully quantified at this stage. Figures 17(b)–(e) shows currents flowing through the system for different configurations (free jet vs. human box) or excitation (sinusoidal vs. pulsed). The size of each current arrow indicates its relative importance qualitatively. Please note that voltages, impedances and currents are time-dependent. Arrows represent currents on average.

The results of this work are discussed, mainly with respect to the proposed electrical equivalent, as follows:

(a) When increasing the peak voltage used (in section 3.1), large variations were observed in RS production for small variations in dissipated power with the human box, but not in free jet. It suggests that the discharge current, which is mainly responsible for RS production, is substantially modified when the target changes. However, its relative importance with regard to displacement current, that also accounts for power dissipation, is low.

This behavior has already been reported by Viegas *et al* [54] and Liu *et al* [55] for a similar plasma jet. In Viegas' work, the displacement current peaks were four times bigger than the discharge current (in free jet and with a floating or grounded target). The target configuration did not influence the displacement current, whereas the discharge current increased with a grounded target.

Figures 17(b) and (c) compares these two situations. The differences can be understood based on the impedances present in the model. The target impedance in free jet is very high, while the total impedance of the human box is between 0.9 and 1 kΩ depending on the frequency. In that regard, the current flowing into the plume (and so also the discharge current in the plume) is substantially increased when using a human box. In nano pulse conditions (with a pulse width of 100 ns), the main frequency component of the applied voltage is estimated at 2 MHz giving a reactance of about 230 Ω for the PTFE wall which is small compared to the impedance of both open-air and the human box. In that regard, the current leaks are similar for both human box and free jet configurations, and the displacement current is relatively stable and relatively important with regard to discharge current.

Globally, it suggests that the system should be electrically designed to limit displacement current and to increase discharge current, i.e. to improve plasma reactivity and limit power dissipation.

(b) When the jet-to-target distance changes (the gas gap at the capillary end), two trends were observed (in section 3.2). For a small gas gap ($d < 1$ cm), the power is dissipated by the plasma in a restricted area, and the gas ionization is high. A longer ionized plasma channel appears when the gas gap lengthens, consuming more power, as observed by Sobota *et al* [56]. However, increasing the gas gap even more ($d > 1.5$ cm) prevents a clear plasma channel (continuous zone of ignited plasma between capillary and target) from being established. The total impedance after the capillary end (including gas gap) increases, leading to lower current and dissipated power. This phenomenon is

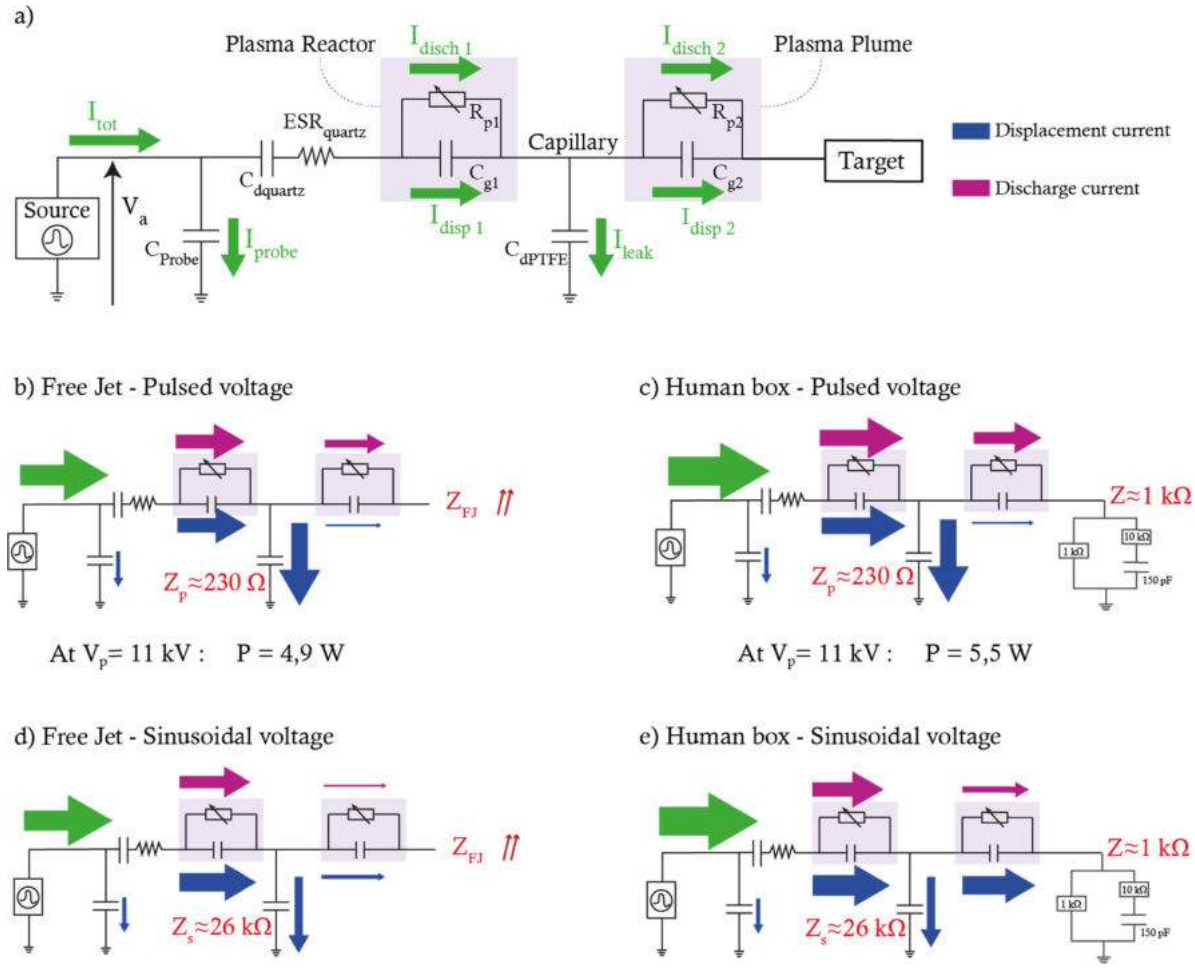

Figure 17. (A) Electrical equivalent circuit approach to explain electrical behaviors observed with measurements. I_{tot} is the input current flowing from the generator to the high-voltage electrode. V_a is the applied voltage. I_{disch} represents the current flowing through the ignited plasma, and I_{disp} represents the current flowing through the system without plasma. I_{probe} is the current through the high voltage probe (with $C_{probe} = 3\ pF$) and I_{leak} represents the current leaks through the PTFE wall. The target corresponds either to the human box (see figure 3) or the air (free jet configuration). C_d, C_g, and R_p are the dielectric capacitance (of quartz and the PTFE tube wall), the gas capacitance (between the quartz wall and the copper rod first, and then between the tip of the copper wire and the target), and the plasma variable resistance (again, at both ends of the copper central rod or wire), respectively. (b), (c), (d) and (e) give schematic representations of current flows through the endoscopic plasma jet depending on the system impedances, to support discussion section. Green arrows represent the total input current, the blue the displacement currents (capacitive) and the pink the discharge currents (conductive).

similar to the free jet configuration, which can be compared to a long gas gap.

(c) When the pulse repetition frequency was increased from 2 to 10 kHz (in section 3.3), the emission intensity of RS proportionally increased. It suggests that no synergetic effect is observed between specific RS production and pulse frequency (within this frequency range), i.e. RS produced by successive pulses do not exceed the sum of those that individual pulses would have produced. Indeed, with such a synergy, called the memory effect [57–60], a present state of the system could depend on a previous event. Hence, a lower energy consumption per pulse would be expected for higher frequencies due to the presence of charged species from the previous discharge. Species known to induce such an effect are leftover electrons, metastable species, and charges accumulated on the dielectric surface. These have different life timescales:

- Nijdam *et al* [61] have shown that leftover electrons strongly impact the subsequent discharges for a time between voltage pulses up to several hundreds of nanoseconds, and that they still can slightly influence the subsequent ignition after several microseconds. As this interval increases, the leftover electrons' impact decreases and ultimately disappears for durations above several dozens of milliseconds, resulting in independent discharges.
- Helium metastable species, with their lifetime of the order of dozens of microseconds [51, 62, 63], can also act as energy reservoirs for electrons or exhibit lower

ionization thresholds, easing the subsequent discharge ignition [59].

- Finally, surface charges accumulating on the dielectric barrier considerably influence subsequent discharges [64]. Indeed, Viegas *et al* have shown that after one microsecond from the previous discharge, the target is partially neutralized, and the remnant deposited charges can stay for at least 200 μs [60].

Therefore, the shortest analyzed time between pulses (i.e. 100 μs corresponding to a 10 kHz frequency) was not short enough to reach the main lifetime timescale (<10 μs) of the species responsible for the memory effect. So, we did not observe it in terms of dissipated power when varying the frequency. However, remnants of those species have longer lifetimes. The longest analyzed time between pulses (i.e. 500 μs corresponding to a 2 kHz frequency) was not long enough to allow the total decay of free electrons and accumulated charges. In that regard, should a memory effect be due to remnants of the species, a similar memory effect would have occurred for all pulse repetition frequencies, also leading to a linear trend.

(d) When the applied voltage pulses were lengthened (in section 3.4), the dissipated power increased while plasma reactivity was unchanged. The first phenomenon that could explain the additional dissipated power is related to current oscillations. After each pulse rise, and as long as the peak voltage is maintained (i.e. between t_1 and t_i in figure 13), the current shows oscillations at around 13 MHz. These could result from a resonance phenomenon with the high voltage wire self-inductance and the system capacitance. The wire self-inductance was estimated at 984 nH (length of 85 cm and diameter of 5 mm) [65]. The system capacitance was estimated at $C_{d-quartz} = 24\ pF$ considering that the whole system is capacitive mainly from the dielectric barrier during the voltage pulse [66]. With those values, the system resonance frequency [67] ($f = 1/\left(2\pi\sqrt{LC}\right)$) is estimated at 33 MHz, relatively close to the observed frequency. Those oscillations mainly correspond to displacement current (as the voltage variations at the top of the voltage pulse are insufficient to induce a discharge) and could dissipate power through dielectric losses, represented by an equivalent series resistance (ESR_{quartz} in figure 17(a)). Consequently, this displacement current dissipates power without the production of emitting species.

The second phenomenon that could explain the additional dissipated power is related to the relatively short time between successive current pulses (hundreds of nanoseconds) within one voltage pulse. In this context, a memory effect could manifest through the presence of electrons in the gas gap (which have a strong influence for a time interval below 1 μs), charge accumulation at the dielectric surface (which are neutralized only after microseconds), or helium metastable species (whose lifetime is dozens of microseconds), easing the ignition of the negative discharge. This would result in a smaller negative discharge current pulse for shorter pulse width, diminishing the power dissipation by the discharge itself.

(e) The current along the tube decreases linearly with the probe position (as observed in section 3.4). Current leakage was already reported upon sinusoidal voltage excitation on a similar system [46]. This previous study has shown that the current flowing in the tube was proportional to the distance between the high voltage electrode and the measurement point, demonstrating a leakage current with a constant value per unit of length (0.06 mA RMS cm^{-1}) in the free jet configuration. This current leak was not observed with an electrical equivalent human body target as its impedance was small enough to offer a preferential path for the current.

In this work, with pulsed voltage, the RMS current decreased along the tube in both configurations with a slope of 0.20 mA cm^{-1}. In free jet, the current loss was smaller with pulsed voltage than with sinusoidal voltage: 30% of the RMS current remained at the end of the tube with pulsed voltage, versus 4% for sinusoidal for the same tube length. This proportion was obtained by taking the ratio of the current at the end of the tube (180 cm from HV electrode) over the current at the beginning (20 cm from HV electrode). In that regard, two major differences can be observed. First, the current leakage profile did not depend on the target for pulsed excitation whereas, for sinusoidal excitation, leakage was nearly not observed with the human box but was quite pronounced in the free jet configuration. Second, in free jet, a larger part of the current remains at the plume for pulsed excitation compared to sinusoidal excitation.

The first observation could be explained by the reactance of the PTFE wall in figures 17(b)–(e). With a sinusoidal voltage applied at 18 kHz (i.e. reported frequency), the reactance is estimated at 26 kΩ for the whole capillary (figures 17(d) and (e)). The human box hence offers a path of lower impedance (i.e. between 0.9 and 1 $k\Omega$ depending on the frequency, see figure 2 for the electrical equivalent) by comparison with the high reactance of the tube walls (i.e. 26 kΩ). For pulsed input voltage (figures 17(b) and (c)), this is no longer the case, as already discussed in point 1 (i.e. the 230 Ω of the tube walls is low compared to the impedance of both open-air and the human box), explaining why current leaks are similar for both human box and free jet configurations.

The second observation could be explained by the impedance of the plume (right pink box in figure 17), which is smaller, on average, for pulsed excitation (figure 17(b)) compared to sinusoidal excitation (figure 17(d)). In that regard, even if there is a smaller reactance of the tube walls, which tends to make current leak out of the device, a larger proportion still reaches the plume. The moments during which displacement and discharge currents flow are important to explain the relative loss of current. With pulsed voltage, no voltage is applied to the system between pulses, and the device has no resulting current, hence no loss. During pulses, a discharge appears, creating a low impedance at the plume (R_{P2} decreases in figure 17(b)), and a large discharge current (I_{disp2} in figure 17(b)) flows. By contrast, a varying voltage is

applied continuously with sinusoidal excitation. It implies that a displacement current continuously flows through the capillary dielectric walls even when plasma is not ignited (hence R_{P2} is large in figure 17(d)). In that regard, the total ratio of discharge current over displacement current is larger with pulsed excitation than with AC excitation, reducing the relative importance of the leaks.

5. Conclusion

The major findings included:

- Target configuration (impedance of target and distance) determines the behavior of the system. It should be considered to design robust medical devices preventing unwanted changes in plasma regime, for example, if the distance between the capillary and the target varies during the treatment.
- The species production can drastically be enhanced with higher peak voltage when in contact with a human body electrical equivalent target. However, power consumption does not reflect this change directly, implying that the system behaves more efficiently. It also implies that by reducing either dielectric losses, or displacement current, it is possible to increase the ratio of plasma reactivity over power consumption.
- No memory effect between pulses was observed in the stationary regime, within the frequency range of 2–10 kHz. Therefore, increasing frequency increases plume intensity and RS production relatively linearly. In future work, other frequency ranges should be explored and initial discharges, before the stationary regime, should be studied.
- Reducing the pulse width from 400 to 100 ns decreases dissipated power without impacting plasma reactivity. This may be explained by a diminution of power losses in the dielectric material and/or by a memory effect easing the second current discharge.
- For a 2 m long plasma jet, pulsed excitation voltage leads to a better discharge current (i.e. producing RS) over displacement current (unwanted for medical applications) ratio, than sinusoidal excitation voltage. For pulsed excitation, leakage currents are similar in free jet and with a human body electrical equivalent target. On the contrary, for sinusoidal excitation, leakage current is larger in the free jet configuration.

Those findings could be of great interest for the cold plasma medicine field where reactive oxygen and nitrogen species are responsible for cell responses, and current administration should be kept low [24, 25, 68]. This behavior should be confirmed in further work with a better model of human tissues [69] or *in vivo*, to assess the cellular responses.

Finally, a detailed electrical equivalent model for a long plasma jet for endoscopy is now needed to deeply understand the electrical behavior of such a medical device and to be able to predict and mitigate risks for the patients and physicians. This will be the object of further investigations.

Data availability statement

The data that support the findings of this study are available upon reasonable request from the authors.

Acknowledgments

This work was funded by the 'Michel Cremer Foundation' and by the Université libre de Bruxelles. The authors acknowledge the contribution of a medical writer, Sandy Field, PhD, for language editing of this manuscript.

ORCID iDs

Orianne Bastin https://orcid.org/0000-0003-4993-3525
Max Thulliez https://orcid.org/0000-0001-9614-3417

References

[1] Fridman G, Friedman G, Gutsol A, Shekhter A B, Vasilets V N and Fridman A 2008 Applied plasma medicine *Plasma Process. Polym.* **5** 503–33
[2] Weltmann K, V. Woedtke T, Vasilets V N, Gutsol A, Shekhter A B and Fridman A 2009 Plasma Medicine *High Energy Chem.* **43** 229–33
[3] Keidar M, Walk R, Shashurin A, Srinivasan P, Sandler A, Dasgupta S, Ravi R, Guerrero-Preston R and Trink B 2011 Cold plasma selectivity and the possibility of a paradigm shift in cancer therapy *Br. J. Cancer* **105** 1295–301
[4] Kalghatgi S U, Fridman G, Fridman A and Friedman G 2008 Non-thermal dielectric barrier discharge plasma treatment of endothelial cells *30th Annual Int. Conf. IEEE Engineering in Medicine and Biology Society* vol 2 pp 3578–81
[5] Hadefi A *et al* 2022 Cold atmospheric plasma differentially affects cell renewal and differentiation of stem cells and APC-deficient-derived tumor cells in intestinal organoids *Cell Death Discov.* **8** 66
[6] Graves D B 2012 The emerging role of reactive oxygen and nitrogen species in redox biology and some implications for plasma applications to medicine and biology *J. Phys. D: Appl. Phys.* **45** 263001
[7] Yan D, Sherman J H and Keidar M 2017 Cold atmospheric plasma, a novel promising anti-cancer treatment modality *Oncotarget* **8** 15977–95
[8] Foster K W, Moy R L and Fincher E F 2008 Advances in plasma skin regeneration *J. Cosmet. Dermatol.* **7** 169–79
[9] Kurosawa M, Takamatsu T, Kawano H, Hayashi Y, Miyahara H, Ota S, Okino A and Yoshida M 2019 Endoscopic hemostasis in porcine gastrointestinal tract using CO_2 low-temperature plasma jet *J. Surg. Res.* **234** 334–42
[10] Metelmann H, von Woedtke T and Weltmann K 2018 *Comprehensive Clinical Plasma Medicine* (Cham: Springer International Publishing) (https://doi.org/10.1007/978-3-319-67627-2)
[11] Rogério P M, Kostov G K and Vadym P 2016 Atmospheric plasma jet device with long distance plasma transfer BR102016005704A2
[12] Bastin O *et al* 2019 Device for cold plasma treatment, cold plasma endoscopic system, and method for generating and transporting a cold plasma *US Patent* EP3914174A1

[13] Vassiliou M C, von Renteln D, Wiener D C, Gordon S R and Rothstein R I 2010 Treatment of ultralong-segment Barrett's using focal and balloon-based radiofrequency ablation *Surg. Endosc. Other Interv. Tech.* **24** 786–91
[14] Altonbary A Y, Galal A, El-Nady M and Hakim H 2019 Endoscopic ultrasound guided biliary drainage: a multicenter retrospective experience of a technique slowly gaining acceptance in Egypt *Therap. Adv. Gastroenterol. Endoscopy* **12** 263177451988945
[15] Kitamura K, Yamamiya A, Ishii Y, Mitsui Y and Yoshida H 2019 Endoscopic side-by-side uncovered self-expandable metal stent placement for malignant hilar biliary obstruction *Therap. Adv. Gastroenterol. Endoscopy* **12** 263177451984634
[16] Cherrington A D, Rajagopalan H, Maggs D and Devière J 2017 Hydrothermal duodenal mucosal resurfacing: role in the treatment of metabolic disease *Gastrointest. Endosc. Clin. North Am.* **27** 299–311
[17] Robert E *et al* 2013 Perspectives of endoscopic plasma applications *Clin. Plasma Med.* **1** 8–16
[18] Winter J, Nishime T M C, Bansemer R, Balazinski M, Wende K and Weltmann K-D 2019 Enhanced atmospheric pressure plasma jet setup for endoscopic applications *J. Phys. D: Appl. Phys.* **52** 024005
[19] Kostov K G, Machida M, Prysiazhnyi V and Honda R Y 2015 Transfer of a cold atmospheric pressure plasma jet through a long flexible plastic tube *Plasma Sources Sci. Technol.* **24** 025038
[20] Thulliez M, Bastin O, Rémy A, Nonclercq A, Devière J, Delchambre A and Reniers F 2022 Effect of gas flow on a helium/oxygen endoscopic plasma jet *J. Phys. D: Appl. Phys.* **55** 415202
[21] Schmidt A and Bekeschus S 2022 How safe is plasma treatment in clinical applications? *Textbook of Good Clinical Practice in Cold Plasma Therapy* (Cham: Springer International Publishing) pp 99–126
[22] Judée F, Vaquero J, Guégan S, Fouassier L and Dufour T 2019 Atmospheric pressure plasma jets applied to cancerology: correlating electrical configuration with *in vivo* toxicity and therapeutic efficiency *J. Phys. D: Appl. Phys.* **52** 245201
[23] Chen Z *et al* 2022 Cold atmospheric plasma delivery for biomedical applications *Mater. Today* **54** 153–88
[24] Gerling T, Bansemer R, Timmermann E and Weltmann K-D 2022 Basic principles and future developments in cold plasma therapy *Textbook of Good Clinical Practice in Cold Plasma Therapy* (Cham: Springer International Publishing) pp 257–80
[25] Nastuta A V and Gerling T 2022 Cold atmospheric pressure plasma jet operated in ar and he: from basic plasma properties to vacuum ultraviolet, electric field and safety thresholds measurements in plasma medicine *Appl. Sci.* **12** 644
[26] Walsh J L, Shi J J and Kong M G 2006 Contrasting characteristics of pulsed and sinusoidal cold atmospheric plasma jets *Appl. Phys. Lett.* **88** 171501
[27] Mildren R P and Carman R J J 2001 Enhanced performance of a dielectric barrier discharge lamp using short-pulsed excitation *J. Phys. D: Appl. Phys.* **34** 1–6
[28] Ayan H, Fridman G, Gutsol A F, Vasilets V N, Fridman A and Friedman G 2008 Nanosecond-pulsed uniform dielectric-barrier discharge *IEEE Trans. Plasma Sci.* **36** 504–8
[29] Benard N and Moreau E 2014 Electrical and mechanical characteristics of surface AC dielectric barrier discharge plasma actuators applied to airflow control *Exp. Fluids* **55** 1846
[30] Rodrigues F, Pascoa J and Trancossi M 2018 Heat generation mechanisms of DBD plasma actuators *Exp. Therm. Fluid Sci.* **90** 55–65
[31] Roth J R, Rahel J, Dai X and Shermann D M 2005 The physics and phenomenology of paraelectric one atmosphere uniform glow discharge plasma (OAUGDP^{TM}) actuators for aerodynamic flow control *J. Phys. D: Appl. Phys.* **38** 555–67
[32] Lu X P and Laroussi M 2006 Temporal and spatial emission behaviour of homogeneous dielectric barrier discharge driven by unipolar sub-microsecond square pulses *J. Phys. D: Appl. Phys.* **39** 1127–31
[33] Laroussi M, Lu X, Kolobov V and Arslanbekov R 2004 Power consideration in the pulsed dielectric barrier discharge at atmospheric pressure *J. Appl. Phys.* **96** 3028–30
[34] Winter J, Nishime T M C, Glitsch S, Lühder H and Weltmann K D 2018 On the development of a deployable cold plasma endoscope *Contrib. Plasma Phys.* **58** 404–14
[35] Gazeli K, Svarnas P, Lazarou C, Anastassiou C, Georghiou G E, Papadopoulos P K and Clément F 2020 Physical interpretation of a pulsed atmospheric pressure plasma jet following parametric study of the UV-to-NIR emission *Phys. Plasmas* **27** 123503
[36] Stancampiano A, Chung T-H, Dozias S, Pouvesle J-M, Mir L M and Robert E 2019 Mimicking of human body electrical characteristic for easier translation of plasma biomedical studies to clinical applications *IEEE Trans. Radiat. Plasma Med. Sci.* **3** 1–23
[37] Judée F and Dufour T 2019 Plasma gun for medical applications: engineering an equivalent electrical target of the human body and deciphering relevant electrical parameters *J. Phys. D: Appl. Phys.* **52** 16LT02
[38] Cheng X, Sherman J, Murphy W, Ratovitski E, Canady J and Keidar M 2014 The effect of tuning cold plasma composition on glioblastoma cell viability *PLoS One* **9** 1–9
[39] Nie Q Y, Cao Z, Ren C S, Wang D Z and Kong M G 2009 A two-dimensional cold atmospheric plasma jet array for uniform treatment of large-area surfaces for plasma medicine *New J. Phys.* **11** 115015
[40] Liu D W, Iza F and Kong M G 2009 Electron avalanches and diffused-mode in radio-frequency capacitively coupled atmospheric-pressure microplasmas *Appl. Phys. Lett.* **95** 031501
[41] Nersisyan G and Graham W G 2004 Characterization of a dielectric barrier discharge operating in an open reactor with flowing helium *Plasma Sources Sci. Technol.* **13** 582–7
[42] Software MATLAB 2019 Matlab R2019a (The MathWorks, Inc.) (Accessed 8 March 2019)
[43] Jahanmiri A, Rahimpour M R, Mohamadzadeh Shirazi M, Hooshmand N and Taghvaei H 2012 Naphtha cracking through a pulsed DBD plasma reactor: effect of applied voltage, pulse repetition frequency and electrode material *Chem. Eng. J.* **191** 416–25
[44] Shao T, Long K, Zhang C, Wang J, Zhang D, Yan P and Zhang S 2009 Electrical characterization of dielectric barrier discharge driven by repetitive nanosecond pulses in atmospheric air *J. Electrostat.* **67** 215–21
[45] Traldi E, Boselli M, Simoncelli E, Stancampiano A, Gherardi M, Colombo V and Settles G S 2018 Schlieren imaging: a powerful tool for atmospheric plasma diagnostic *EPJ Tech. Instrum.* **5** 1–23
[46] Bastin O, Thulliez M, Servais J, Nonclercq A, Delchambre A, Hadefi A, Devière J and Reniers F 2020 Optical and electrical characteristics of an endoscopic DBD plasma jet *Plasma Med.* **10** 71–90
[47] Höft H, Kettlitz M, Becker M M, Hoder T, Loffhagen D, Brandenburg R and Weltmann K-D 2014 Breakdown characteristics in pulsed-driven dielectric barrier discharges: influence of the pre-breakdown phase due to volume memory effects *J. Phys. D: Appl. Phys.* **47** 465206
[48] Pipa A V and Brandenburg R 2019 The equivalent circuit approach for the electrical diagnostics of dielectric barrier

discharges: the classical theory and recent developments *Atoms* **7** 14
[49] Manley T 1943 The electric characteristics of the ozonator discharge *Eighty-Fourth General Meeting* pp 83–96
[50] Liu S and Neiger M 2001 Excitation of dielectric barrier discharges by unipolar submicrosecond square pulses *J. Phys. D: Appl. Phys.* **34** 1632–8
[51] Douat C, Kacem I, Sadeghi N, Bauville G, Fleury M and Puech V 2016 Space-time resolved density of helium metastable atoms in a nanosecond pulsed plasma jet: influence of high voltage and pulse frequency *J. Phys. D: Appl. Phys.* **49** 285204
[52] Yehia A 2016 The electrical characteristics of the dielectric barrier discharges *Phys. Plasmas* **23** 063520
[53] Liu S and Neiger M 2003 Electrical modelling of homogeneous dielectric barrier discharges under an arbitrary excitation voltage *J. Phys. D: Appl. Phys.* **36** 3144–50
[54] Viegas P, Hofmans M, van Rooij O, Obrusník A, L M Klarenaar B, Bonaventura Z, Guaitella O, Sobota A and Bourdon A 2020 Interaction of an atmospheric pressure plasma jet with grounded and floating metallic targets: simulations and experiments *Plasma Sources Sci. Technol.* **29** 095011
[55] Liu Y, Qi H, Fan Z, Yan H and Ren C S 2016 The impacts of magnetic field on repetitive nanosecond pulsed dielectric barrier discharge in air *Phys. Plasmas* **23** 113508
[56] Sobota A, Guaitella O and Rousseau A 2014 The influence of the geometry and electrical characteristics on the formation of the atmospheric pressure plasma jet *Plasma Sources Sci. Technol.* **23** 025016
[57] Tyl C, Lin X, Bouzidi M C, Dap S, Caquineau H, Ségur P, Gherardi N and Naudé N 2018 Investigation of memory effect in atmospheric pressure dielectric barrier discharge in nitrogen with small oxygen or nitric oxide addition *J. Phys. D: Appl. Phys.* **51** 354001
[58] Pan C, Wu K, Chen G, Gao Y, Florkowski M, Lv Z and Tang J 2020 Understanding partial discharge behavior from the memory effect induced by residual charges: a review *IEEE Trans. Dielectr. Electr. Insul.* **27** 1951–65
[59] Zhao Z and Li J 2020 Repetitively pulsed gas discharges: memory effect and discharge mode transition *High Volt.* **5** 569–82
[60] Viegas P, Slikboer E, Bonaventura Z, Garcia-Caurel E, Guaitella O, Sobota A and Bourdon A 2022 Quantification of surface charging memory effect in ionization wave dynamics *Sci. Rep.* **12** 1181
[61] Nijdam S, Teunissen J and Ebert U 2020 The physics of streamer discharge phenomena *Plasma Sources Sci. Technol.* **29** 103001
[62] Tochikubo F, Chiba T and Watanabe T 1999 Structure of low-frequency helium glow discharge at atmospheric pressure between parallel plate dielectric electrodes *Jpn. J. Appl. Phys.* **38** 5244
[63] Massines F, Ghérardi N, Naudé N and Ségur P 2009 Recent advances in the understanding of homogeneous dielectric barrier discharges *Eur. Phys. J. Appl. Phys.* **47** 1–10
[64] Zhao Z, Huang D D, Wang Y N, Li C J and Li J T 2020 Volume and surface memory effects on evolution of streamer dynamics along gas/solid interface in high-pressure nitrogen under long-term repetitive nanosecond pulses *Plasma Sources Sci. Technol.* **29** 015016
[65] Rawlins J C 2000 Inductance and transformers *Basic AC Circuits* (London: Newnes) pp 257–302
[66] Rawlins J C 2000 Capacitance *Basic AC Circuits* (London: Newnes) pp 171–215
[67] Rawlins J C 2000 Resonance *Basic AC Circuits* (London: Newnes) pp 453–87
[68] Weltmann K-D, Kindel E, Brandenburg R, Meyer C, Bussiahn R, Wilke C and von Woedtke T 2009 Atmospheric pressure plasma jet for medical therapy: plasma parameters and risk estimation *Contrib. Plasma Phys.* **49** 631–40
[69] Thulliez M, Bastin O, Nonclercq A, Delchambre A and Reniers F 2021 Gel models to assess distribution and diffusion of reactive species from cold atmospheric plasma: an overview for plasma medicine applications *J. Appl. Phys.* **54** 463001